Assessment of Machine Learning Approaches for Bathymetry Mapping in Shallow Water Environments using Multispectral Satellite Images

Mohamed, H. and Nadaoka, K.
Department of Transdisciplinary Science and Engineering, Tokyo Institute of Technology, Tokyo, Japan
E-mail: hussein.h.aa@m.titech.ac.jp

Abstract
This paper evaluates the performance of two proposed empirical approaches—random forest (RF) and multi-adaptive regression spline (MARS)—for bathymetry calculations in three diverse areas: the Alexandria harbor shallow coastal area, Egypt, as an example of a low-turbidity, silt-sand bottom water area with depths ranging from 4 m to 10.5 m; the Lake Nubia entrance zone, Sudan, which is considered a high-turbidity, unstable, clay bottom area with a depth of 6 m; and Shiraho, Ishigaki Island, Japan, a coral reef area with a depth of 14 m. Data from Landsat 8 and Spot 6 satellite images were used to evaluate the performance of the proposed models. The bathymetry results of the proposed models were compared with the corresponding results yielded from two conventional empirical methods: the neural network (NN) model and the Lyzenga generalized linear model (GLM). When compared with echo sounder data, the RF and MARS results outperformed Lyzenga GLM results. Moreover, the RF method produced more accurate results with average 0.25 m RMSE improvements range than the NN model. The RF algorithm produced the most accurate results proved to be a preferable algorithm for bathymetry mapping in the shallow water context.

1. Introduction

Coastal and lake shallow areas bathymetry is significant for many purposes and applications, such as coastal engineering sciences, spatial monitoring of lakes, and sustainable management of natural resources (Leu and Chang, 2005 and Gao, 2009). In addition, sediments deposition and erosion in these shallow areas are rapid because of tidal currents, wave propagation and intensive human activities (Ceyhun and Yalçın, 2010). Accordingly, accurate and updated monitoring measurements of these areas, particularly water depths, need to be performed (Pacheco et al., 2015).

Currently, single and multibeam echosounders besides Lidar represent the conventional methods for bathymetry applications. The multibeam echosounder is especially useful for very deep waters with depths of up to 500 m due to its higher accuracy and full bottom coverage. Alternatively, the single-beam echosounder can produce sea bottom maps with adequate vertical accuracy at a lower cost than the multibeam echosounder (Sánchez-Carnero et al., 2014). However, despite their high level of depth accuracy, these systems are costly and difficult to use, especially in shallow areas where coral reefs, rocks, and general shallowness are an obstacle to the navigation of survey vessels (Chust et al., 2010). Recently, airborne Lidar technology has been developed for bathymetry applications. However, both these techniques are expensive, time-consuming, require exhaustive labor, and have comparatively low coverage.

Optical satellite images represent a low-cost, wide-coverage, and time-effective alternative to conventional methods for bathymetry applications (Sánchez-Carnero et al., 2014). According to the literature review, two approaches have been used for bathymetry retrieval: analytical and empirical. Analytical approaches are complex and require spectral data for bottom reflectance, and dissolved or suspended matter in the water column (Vahtmäe and Kutser, 2016). In contrast, empirical approaches depend on the relation between the reflectance of the water body and water depths in sample locations, which makes these methods simpler. Lyzenga (1985) developed a log-linear empirical method for extracting water depths from satellite images. His theory was dependent on performing a log-linear correlation between single or multiple bands and water depth values (Sánchez-Carnero et al., 2014). This approach was applied successively by other researchers using diverse satellite images: Quickbird (Lyons et al., 2011), Worldview-2 (Doxani et al., 2012), and Landsat 8 (Pacheco et al., 2015). A different empirical method dependent on band ratios, in which the difference in attenuation

for two bands can be used for extracting data on water depth, was developed by Stumpf (2003). Recently, Stumpf's approach has been further developed by other researchers such as Su et al., (2008) and Bramante et al., (2013). These two methods are considered the most widely used empirical algorithms for bathymetry data retrieval (Vahtmäe and Kutser, 2016).

Recently, Ceyhun and Yalçın (2010) proposed a novel alternative approach for detecting water depths using the neural network (NN) algorithm. NNs perform a nonlinear relation between satellite image spectral bands and water depth values, overcoming the limitations of regressive models. Successively, many researchers have proved the precedence of NN algorithms to conventional approaches using different satellite images, for example, Landsat images (Gholamalifard et al., 2013) and IRS P6-LISS III images (Moses et al., 2013). Moreover, Quickbird images (Corucci, 2011) using a neuro-fuzzy approach.

However, the abovementioned three approaches have various limitations. The Lyzenga approach assumes that the bottom surface is entirely homogenous and that the water column is similar in the whole coverage area. Stumpf's approach overcomes this demerit; however, it has no physical basis and its parameters are calculated through a trial process (Gholamalifard et al., 2013). Finally, the NN method has many weaknesses such as a complex black-box nature; sensitivity to any small change in the input data values, resulting in high differences in output results; and its vulnerability to over fit the bathymetry data.

This study proposes two new approaches for bathymetry detection in shallow coastal or lake areas and endeavors to overcome the disadvantages of the NN and Lyzenga generalized linear model (GLM) methods. These approaches are the random forest (RF) and the multi-adaptive regression spline (MARS) methods. These algorithms are more stable and more invincible to overfitting than NN, simpler than analytical approaches, and less affected by other environmental factors than Lyzenga GLM. The proposed bathymetry methodologies were applied using Spot 6 and Landsat 8 images. The achieved bathymetry results are then evaluated and compared with echosounder bathymetry data over three study areas.

2. Study Areas and Available Data

2.1 Study Areas

The first study area is Alexandria harbor, Egypt (Figure 1a). It is a deep, low-turbidity, calm water area, because of its coastal barriers, and has a depth of 10.5 m. almost the entire port bottom surface cover is the silt-sand area. The second study area is the entrance zone of Lake Nasser (Egypt) or Lake Nubia (Sudan), which is located in Sudan (Figure 1b). It is an irregular, shallow, the high turbid water area with depths of up to 6 m and high rates of sediment variation and annual flood changes. The lake has a clay bottom surface. The third study area is Shiraho, a subtropical territory located in the southeastern part of Ishigaki Island, Japan (Figure 2). It is an irregular heterogeneous shallow, low-turbidity water area with depths of up to 14 m. The Shiraho area has a rich marine biodiversity, which includes various ecosystems such as seagrasses and coral reefs, fish species, and the world's largest colony of rare Blue Ridge coral (Heliopora coerulea).

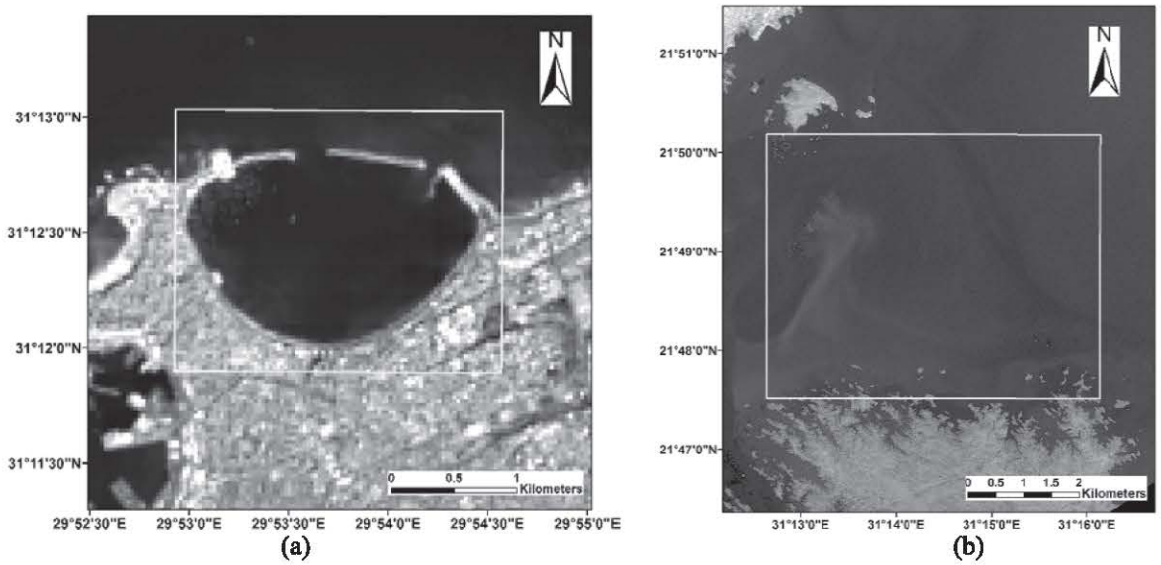

Figure 1: a) The 1st study area of Alexandria port coastal area, Egypt, b) The 2nd study area of Nubia Lake

Figure 2: The 3rd study area of Shiraho, Ishigaki Island, Japan

2.2 Imagery Data

Freely available Landsat 8 satellite images, having a spatial resolution of 30 m, were used for detecting the bathymetry for the first and third study areas. Spot 6 satellite images with 1.5 m spatial resolution were used for the second study area. The required parameters for radiometric image corrections were available in metadata files of the images.

The first image of the Alexandria harbor was acquired during calm weather conditions on March 22, 2014. The second image of Sudan was collected during windy conditions on January 12, 2014. The third image of Shiraho was acquired during calm weather conditions on June 5, 2013. These images were selected to be synchronized with the echosounder field collection times for each study area.

2.3 Echo-Sounder-Benthic Cover Field Data

The reference water depths of the first study area were used for calibrating the algorithms acquired from a NaviSound Hydrographic Systems model 210 echosounder instrument with an attached Trimble 2000 GPS (Figure 3a). The maximum depth range of the echosounder was 400 m, and its vertical accuracy was 1 cm at 210 kHz. The reference water depths of the second study area were acquired with an Odom Hydrographic Systems Echotrac model DF 3200 MKII echosounder instrument with built-in differential GPS (Figure 3b). The depth range of the echo sounder were 0.2–200 m and its vertical accuracy was 0.01 m ± 0.1% of depth. Finally, the reference water depths of the third study area were acquired from Collin et al., (2014) using a single-beam Lowrance LCX-15MT dual-frequency (50/200 kHz) transducer and a 12-channel GPS antenna (Figure 4). The horizontal and vertical accuracies were ±1 m and ±0.03 m, respectively (Heyman et al., 2007).

Almost 2500 field points were collected for the first study area, 12500 for the second study area, and 14500 for the third study area. All water depths were referenced to the mean sea level. These points were used for calibration and evaluation of the bathymetry models.

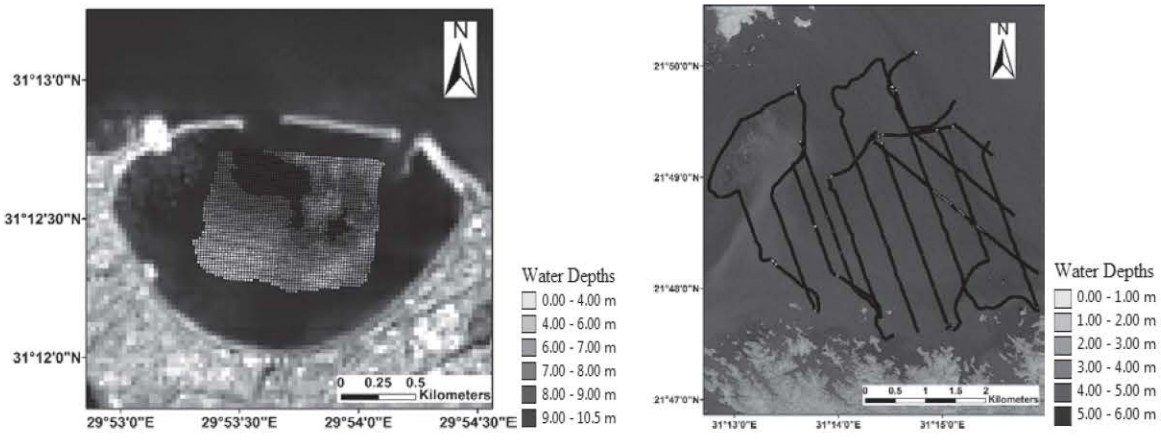

Figure 3: a) Field bathymetry reference points of the 1st study area from echo-sounder b) In-situ bathymetry reference points of the 2nd study area from echo-sounder

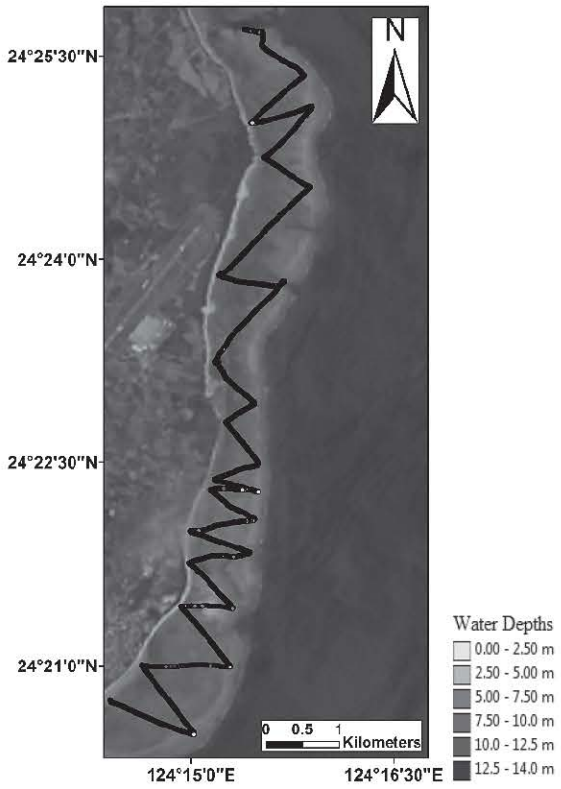

Figure 4: Field bathymetry Reference points of the 3rd study area from echo-sounder

3. Methodology

Several preprocessing operations were completed for the bathymetry estimation of water depths from Landsat 8 and Spot 6 images. First, the images were radiometrically corrected and converted to radiance values. Second, Landsat 8 and Spot 6 bands were atmospherically corrected and converted to reflectance. Third, the images were corrected for the sun glint errors, and then, segmented into land and water areas. The reflectance values were extracted at the same location as that of the reference sounding points. These points were separated into two independent samples with 75% training points and 25% testing points. For example, in the Shiraho study area, sounding points were divided into 10875 training points and 3625 testing points. Each algorithm was trained with red, green, blue/red ratio, and green/red ratio band values as inputs and the sounding values as outputs. Fourth, independent testing points were used for an evaluation of the algorithms based on RMSE, R^2, and mean absolute error (MAE) values. Finally, the bathymetry maps were produced using the trained algorithms. The proposed method consists of several key procedures, as shown in Figure 5, and has been discussed in detail throughout this paper.

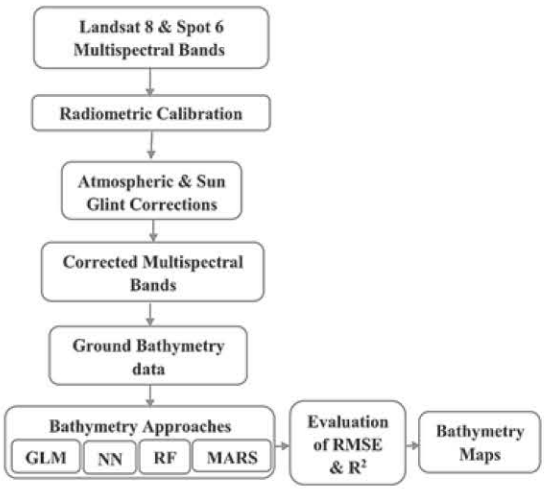

Figure 5: Workflow processing steps for detecting bathymetry from Spot 6 and Landsat 8 satellite images

3.1 Imagery Data Pre-Processing

The determination of bathymetric or benthic information from the satellite images needs first the conversion of images pixel values to radiometrically correct spectral radiance values (Updike and Comp, 2010). The required data for this conversion were available in the images metadata files (MTL files). Also, two essential successive corrections should be applied to the radiance images: the atmospheric correction and the sun glint correction (Doxani et al., 2012). The sequence of these two corrections is optional (Kay et al., 2009). The description of imageries data pre-processing is illustrated in the following subsections.

3.1.1 Spectral top of atmosphere radiance

The digital number pixel values were converted to the spectral top of atmosphere radiance values for each pixel using the following equation (Landsat, 2013):

$$L_\lambda = M_l * DN + A_l \quad \text{Equation 1}$$

Where L_λ = top of atmosphere spectral radiance, DN = digital number recorded by the sensor, M_l = band-specific multiplicative rescaling factor for radiances, and A_l = band-specific additive rescaling factor for radiances. Both M_l and A_l values were available in the images' MTL files.

3.1.2 Atmospheric correction

Atmospheric correction was applied to Landsat 8 and Spot 6 images using the Fast Line-of-Sight Atmospheric Analysis of Hypercubes (FLAASH™) tool in the ENVI 5.3 program. Many previous researchers have used the FLAASH module for atmospheric correction, especially for bathymetry or benthic mapping (Lyons et al., 2011, Blakey et al., 2015 and Wahidin et al., 2015). The calculated radiance images were used as input for the FLAASH tool. FLAASH develops radiative transfer-based models based on the MODTRAN4 code (Berk et al., 1998) and includes look-up tables for different categories of atmospheric conditions. In addition, the FLAASH tool has different types of aerosol models, which define the particle properties such as scattering, absorption, and wavelength path radiance effects. For the three coastal and lake study areas, the maritime were selected as aerosol model type, tropical as the atmospheric model for hot areas. In addition, blue and infrared bands over water were selected as aerosol retrieval (Su et al., 2008). Finally, the atmospherically corrected surface reflectance images were produced.

3.1.3 Sun glint correction

The literature review presents many methods that can be used for correcting the sun glint in the images (Kay et al., 2009). Hedley et al., (2005) method is considered to be the most popular method for sun glint removal. It uses the relation between the bands used for bathymetry and a near-infrared (NIR) band (Hedley et al., 2005 and Sánchez-Carnero et al., 2014). Sun glint correction was applied to the atmospherically corrected surface reflectance images. The de-glinted pixel values can be easily calculated using a sample of pixels according to Equation 2:

$$R_{i'} = R_i * b_i (R_{NIR} - Min_{NIR}) \quad \text{Equation 2}$$

Where $R_{i'}$ = de-glinted pixel reflectance value, R_i = atmospherically corrected reflectance value, bi = regression line slope, R_{NIR} = corresponding pixel value in the NIR band, and Min_{NIR} = min NIR value existing in the sample.

3.2 Proposed Algorithms for Bathymetry Mapping

3.2.1 Random forest

RF is an ensemble of numerous decision trees produced by learning sample groups collected independently from a training set (Breiman, 2001). The training of the RF algorithm is performed by creating multiple decision trees, where each tree is trained on a bootstrapped sample of the training data with replacement for the each tree. The advantage of the RF method is that each node will be split using the best among a subset of predictors randomly chosen at each node (Kim and Sohn, 2011). As a result of random feature selection, the overall accuracy improves in comparison to other methods such as NN; the variation between the sample trees is ensured; and over-fitting of the model to the underlying relation is avoided. Finally, the prediction is estimated using the majority voting technique (Ghimire et al., 2012). RF implementation requires three parameters: the number of input features, the number of variables used to split each node, and the number of grown trees (Guan et al., 2012). Bootstrap samples are collected from a certain percentage of the training dataset and the remaining percentage of calibration samples are called out-of-bag data.

The out-of-bag data are used to estimate the classification accuracy. For regression problems, the splitting percentage is 2/3 of the overall data. Conversely, in classification problems, setting the number of variables equal to the square root of the overall number of variables generally gives the most accurate results (Breiman, 2001). An impurity or error node criterion must also be assigned for splitting each node, such as in the instance of the Gini diversity index. Once the Gini index reaches zero, the resultant node becomes a pure node and one class is assigned for each final node; otherwise the splitting will not be continuous. Many researchers confirmed the outperformance of RF method to other machine learning algorithms in Remote Sensing applications. As instance, Sonobe et al., (2014) presented the better performance of RF algorithm for crop type classification using multi-temporal TerraSAR-X dual- polarimetric data. RF produced 0.93 overall accuracy which was superior to the classification trees with only 0.91 overall accuracy. Moreover, Adam et al., (2014) proved the outperformance of RF algorithm compared to Support Vector Machines (SVM) in land use/cover classification. The comparison was performed over a heterogeneous coastal landscape using RapidEye imagery. A thematic map was produced with 93.7% and 91.8 % overall accuracy from RF and SVM, respectively. This research attempts to use the RF methodology for bathymetry applications for the first time.

3.2.2 Multi-adaptive regression spline

MARS is a multivariate, piecewise-regression, non-parametric technique introduced by Friedman. It is a flexible statistical method for fitting relations between a set of input variables and dependent variables (Kisi and Parmar, 2016).

The basic idea of MARS involves partitioning the training datasets into regions, and then, generating a linear regression equation for each of these regions. This linear regression predictors for each region are called the "basis functions" (BFs). In addition, the end value of a region is the beginning of another and the connection break points between regions are called "knots" (Conoscenti et al., 2015) as shown in Figure 6.

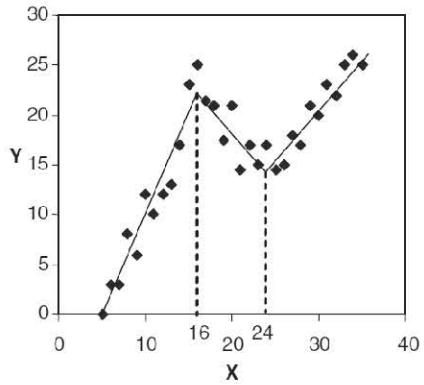

Figure 6: Knots and linear splines for a simple MARS example (Zhou and Leung, 2007)

The piecewise-linear BFs of the following forms represent the basic principle of the MARS technique (Emamgolizadeh et al., 2015):

$$Y = \max(0, X - c) = \begin{cases} X - c & X > c \\ 0 & X \le c \end{cases},$$

$$Y = \max(0, c - X) = \begin{cases} c - X & X < c \\ 0 & X \ge c \end{cases}$$

Equation 4

Where X = the input variables, Y= the output variables, and c = the connection knots or the intersection between successive splines. The MARS model is generated as a linear combination of these basis functions, as follows (Emamgolizadeh et al., 2015):

$$Y = \beta_o + \sum_{i=1}^{M} \beta_i \, Bi(X)$$

Equation 5

Where β_o = the bias, Bi (X) = the BFs, and β_i = the coefficients of BFs, which are calculated by a least square method. Finally, M = the final terms of the model, calculated after two successive steps.

The first step of the MARS is the forward selection procedure performed on the training data. A model is constructed with only the intercept, β_o, and the (BFs) that produce the largest decrease in the training error by the least squares method are added. The addition of the BFs is continued until the model reaches a user-defined maximum number of BFs or the minimum sum square error. The forward step leads to a purposely over a fit model that can predict the training data very well but cannot be generalized for the overall dataset (Zhang et al., 2015). Next, a second step or the backward step begins. The backward step prunes the model by eliminating the BFs with the lowest contribution until reaching an optimal model. To overcome overfitting, a generalized cross-validation (GCV) method is used as a goodness-of-fit test that penalizes large numbers of BFs (Haleem et al., 2013). Finally, the best model with the lowest GCV value is the final MARS model (Hastie et al., 2009).

The MARS model has many advantages compared to more flexible linear models including a capability to generate robust models, no requirements for data preparations or assumptions, and finally, a superior computational efficiency (Zhang and Goh, 2013). Recently, the MARS algorithm has been used for a range of civil engineering and remote sensing research topics (Gharineiat and Deng, 2015 and Kuter et al., 2016) but has not yet been applied for use in bathymetry detection. For instance, Gharineiat and Deng (2015) used MARS method to combine sea level data from altimetry with the high temporal sampling at tide gauges for monitoring extreme sea level measures. To prove the precedence of MARS model it was compared to the multivariate regression model. The results confirmed the superiority of MARS method with 8.21 cm RMSE and 0.62 R^2. However, the multivariate regression model produced 6.73 cm RMSE and 0.44 R^2. In addition, Kuter et al., (2016) confirmed the outperformance of MARS model for the estimation of subpixel snow-covered area compared to Artificial Neural Network (ANN) method. The produced results showed that MARS model performed better than the ANN model with RMSE of 0.17 m over the test areas; whereas the ANN model produced RMSE of 0.38 m.

3.2.3 Neural network

Artificial NNs have been widely used for various remote-sensing applications as an approach to solving classification and regression problems (Mather and Tso, 2009). The multilayer perception (MLP) model using the back propagation (BP) procedure is an NN-supervised approach. It is widely used in demonstrating nonlinear relationships between input and output data (Rumelhart et al., 1986). The MLP model consists of three main parts: an input layer, with a pre-defined number of neurons representing the available dataset; a hidden layer, which controls the

network training and performance process; and an output layer, which presents the output results. The BP algorithm is an iterative process that starts with the initial network weights to find the least error values through comparing actual outputs with the desired values, until a pre-defined level of accuracy is reached (Razavi, 2014). The Levenberg–Marquard training algorithm is used for training the BP process for weight and bias value updating. The BP with the Levenberg–Marquard algorithm is highly recommended for training moderate-sized feed-forward NNs (Ranganathan, 2004). Finally, the log sigmoid function is used for transferring net inputs to node outputs because its derivative is easily computed and commonly used (Ceyhun and Yalçın, 2010).

3.2.4 Lyzenga generalsied linear model

Lyzenga (1985) used a combination of two bands to overcome the drawbacks of using a single-band linear correlation between reflectance and depths values, which assumes that the water column is uniform and that the bottom surface is homogenous. Moreover, Lyzenga et al., (2006) generalized this approach by using more than two bands and argued that it results in data for water depths that are not influenced by other factors such as water column and bottom type. As a result, the water depths can be calculated using Equation 6 (Lyzenga et al., 2006):

$$Z = a_o + \sum_{i=1}^{N} a_i X_i$$

Equation 6

Where Z = the water depth, a_o and a_i = coefficients determined through multiple regression using the reflectance of the corresponding bands and the known depth, and Xi = the logarithm of the corrected band. Recently, many researchers (Doxani et al., 2012 and Sánchez-Carnero et al., 2014) have used Lyzenga GLM to link a linear combination of image bands to the water depth values. GLM represents a least-squares fit response connection to the data (Gentle et al., 2012).

4. Results

Both Landsat 8 and Spot 6 multispectral images of the study areas were pre-processed for bathymetry mapping by converting the image pixel values to radiance using the MTL file values. In addition, the atmospheric and sun glint corrections to the image radiance values were performed. All steps were completed using the ENVI 5.3 interface. The FLAASH tool was used for atmospheric correction and the input parameters were set as described in the methodology for both the coastal tropical and maritime areas.

The resultant images from the atmospheric correction were checked using field signal curves for each reflectance value.

For bathymetry mapping, the proposed approaches of RF and MARS were applied to the pre-processed Landsat 8 and Spot 6 multispectral images and compared with the NN and GLM methods. GLM resulted in the following equations for each of the three study areas:

$$Z_{\text{Alex port}} = 17.25 - 4.69\ L_G - 0.51\ L_R + 0.06\ B/R - 0.10\ G/R + 0.65\ L_G L_R - 0.03\ L_G B/R - 2.30\ L_R G/R + 0.06\ L_G G/R + 0.004\ B/R G/R$$

Equation 7

$$Z_{\text{Nubia lake}} = 2912.2 - 904.96\ L_G + 1219.7\ L_R - 3024.6\ B/R - 1900.7\ G/R + 19.35\ L_G L_R - 1.06\ L_G B/R + 1.07\ L_R G/R - 18.44\ L_G G/R - 1281.1\ L_R B/R + 2143.8\ B/R G/R$$

Equation 8

$$Z_{\text{Shiraho}} = -15.185 + 29.67\ L_G - 39.73\ L_R - 10.48\ B/R + 73.43\ G/R + 0.44\ L_G L_R + 28.63\ L_G B/R - 15.2\ L_R G/R + 5.09\ L_G G/R - 18.22\ L_R B/R + 3.36\ B/R G/R$$

Equation 9

Where L_G is the logarithm of corrected green band, L_R is the logarithm of corrected red band, B/R is blue/red, and G/R is green/red logarithm ratio values.

The parameters of the MARS model were 40 maximum BFs in the forward phase before being pruned in the backward phase. The GCV value was set as 4, which can cope with the recommended value from the simulation studies (Friedman, 1991) and the linear piecewise modeling type. On the other hand, the NN training function was Levenberg–Marquardt BP with 10 hidden layers. Finally, the RF model was constructed with two combined ensembles of 50 regression trees. All of these parameters for each algorithm were selected on the basis of the minimum RMSE and highest R^2 values. These algorithms were implemented in the Matlab environment and the MARS model was implemented with Jekabson's toolbox (Jekabsons, 2016).

Figures 7, 9, and 11 show the bathymetry maps computed by applying each model using the Landsat 8 and Spot 6 satellite images for each study area, Figures 8, 10, and 12 present the evaluation of each model, and Tables 1, 3, and 5 summarize the corresponding RMSE, R^2, and MAE values. Moreover, Tables 2, 4, and 6 demonstrate the obtained depths in each of the three study area ranges for each method.

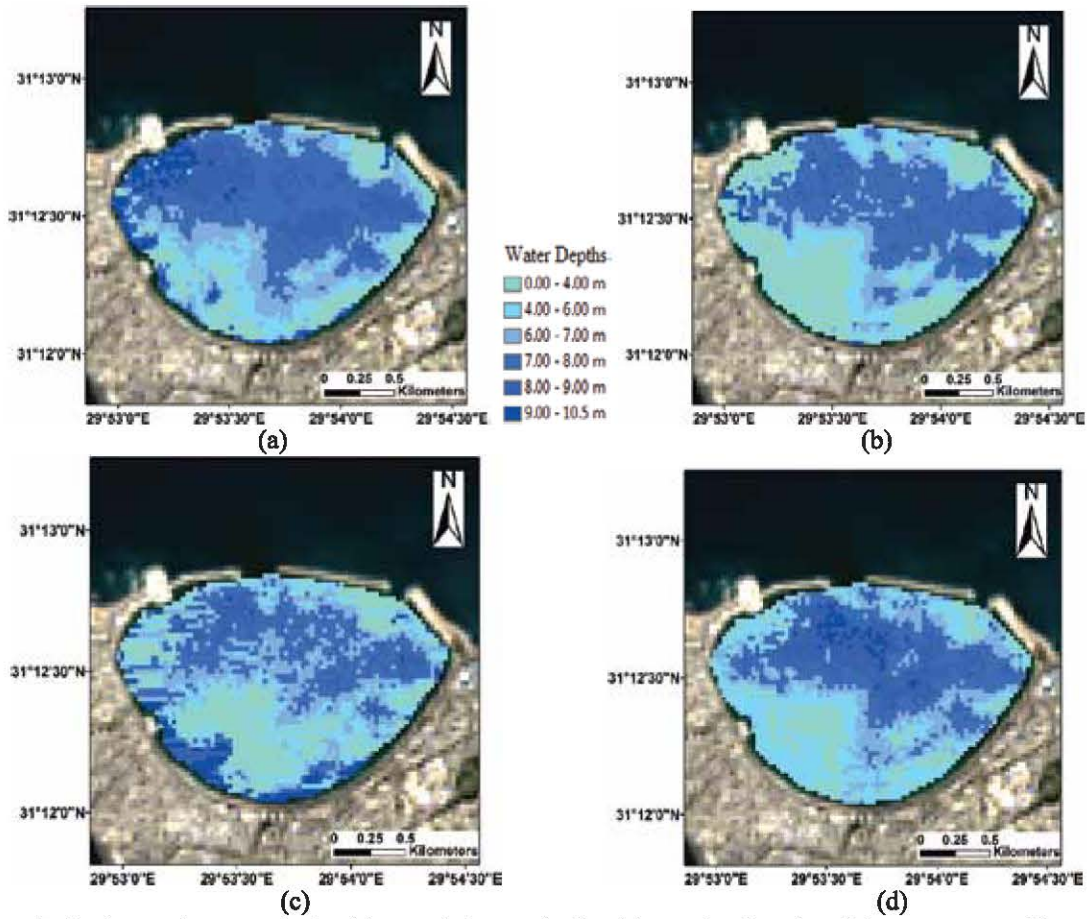

Figure 7: Bathymetric maps derived by applying each algorithm using Landsat-8 imagery over Alexandria harbor area, Egypt. (a) GLM (b) NN (c) MARS (d) RF

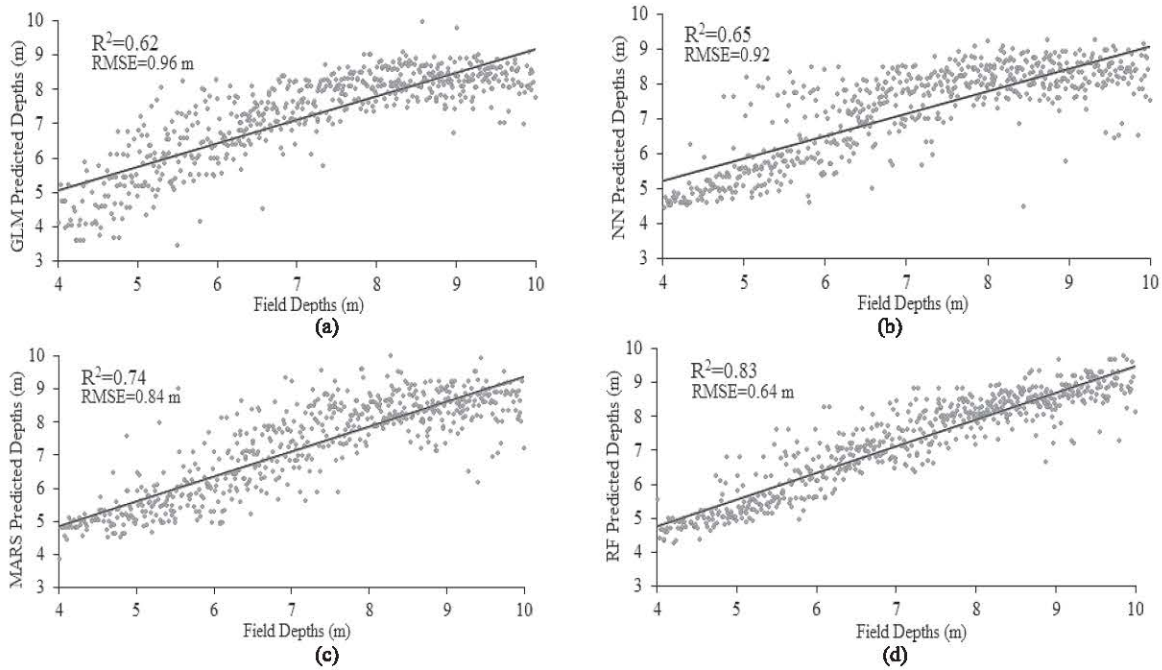

Figure 8: The continuous fitted models for Alexandria port area, Egypt. Depths are represented as points, and the continuous line represents the continuous fitted model (a) GLM (b) NN (c) MARS (d) RF

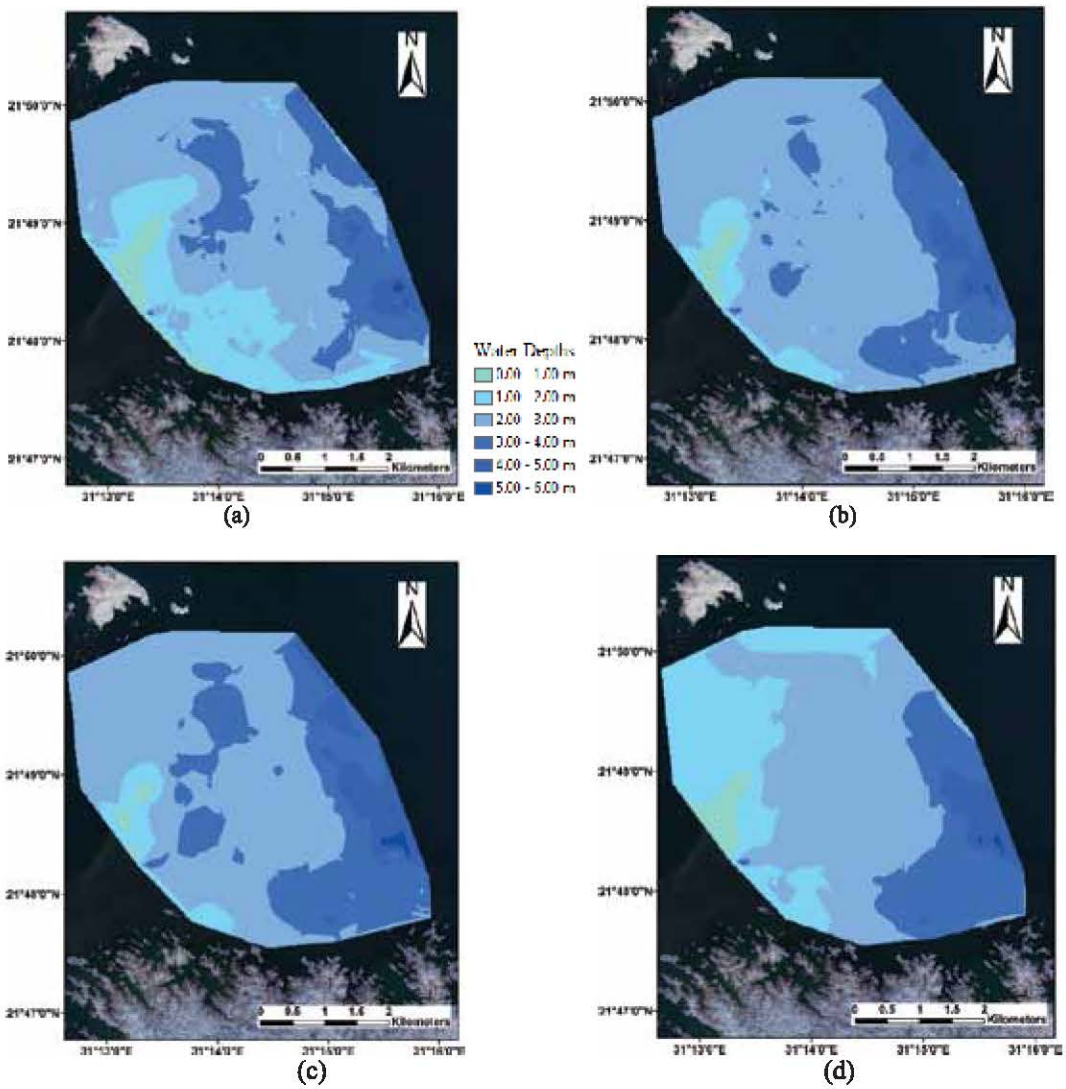

Figure 9: Bathymetric maps derived by applying each algorithm using Spot 6 imagery over Nubia Lake entrance zone, Sudan. (a) GLM (b) NN (c) MARS (d) RF

Table 1: The RMSEs, R^2, and MAE of all methods for bathymetry detection over Alexandria port area, Egypt

Methodology	GLM	NN	MARS	RF
RMSE (m)	0.96	0.92	0.84	0.64
R^2	0.62	0.65	0.74	0.83
MAE	0.74	0.62	0.65	0.49

Table 2: The RMSEs (in meters) of all bathymetry detection methods in three ranges of depths for Alexandria port area, Egypt

Methodology	GLM	NN	MARS	RF
4-6 m	1.03	0.84	0.77	0.63
6-8 m	0.74	0.94	0.87	0.62
8-10.5 m	0.99	0.98	0.88	0.67

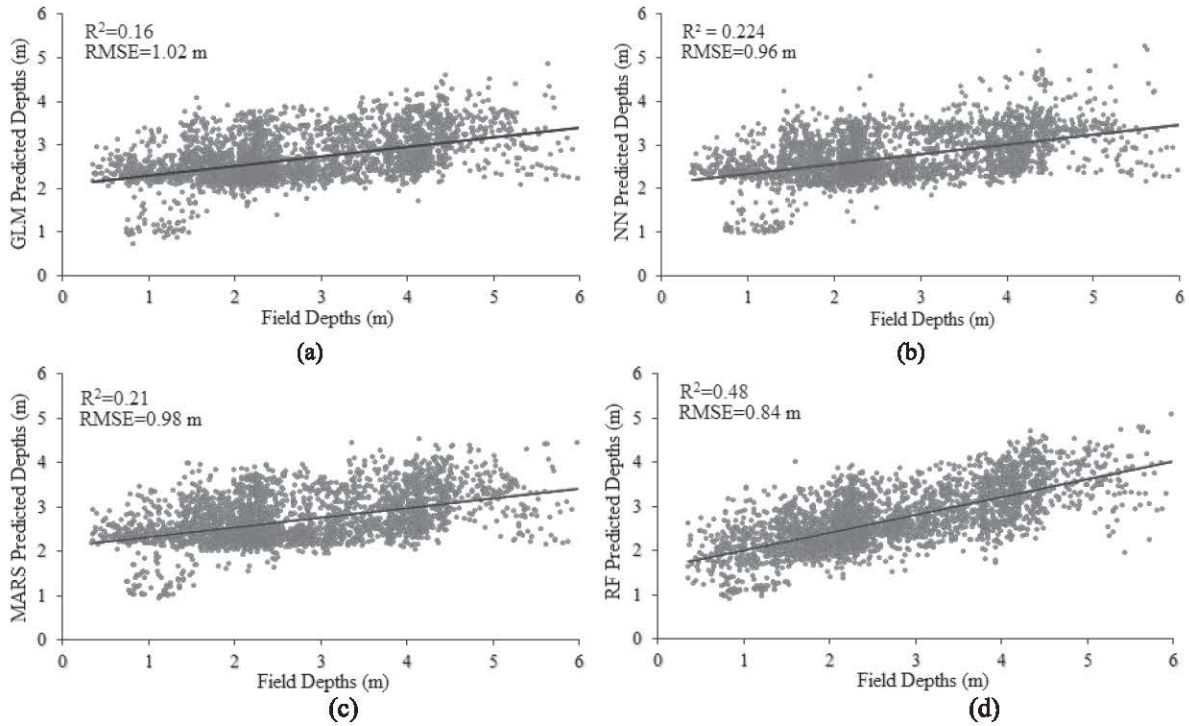

Figure 10: The continuous fitted models for Nubia Lake entrance zone, Sudan. Depths are represented as points, and the continuous line represents the continuous fitted model (a) GLM (b) NN (c) MARS (d) RF

Table 3: The RMSEs, R^2, and MAE of all methods for bathymetry detection for Nubia Lake entrance zone, Sudan

Methodology	GLM	NN	MARS	RF
RMSE (m)	1.02	0.96	0.98	0.84
R^2	0.16	0.23	0.21	0.48
MAE	0.84	0.80	0.81	0.63

Table 4: The RMSEs (in meters) of all bathymetry detection methods in three ranges of depths for Nubia Lake entrance zone, Sudan

Methodology	GLM	NN	MARS	RF
0-2 m	0.92	0.88	0.91	0.74
2-4 m	0.94	0.93	0.93	0.76
4-6 m	1.99	1.63	1.77	1.31

Table 5: The RMSEs, R^2, and MAE of all methods for bathymetry detection for Shiraho Island, Japan

Methodology	GLM	NN	MARS	RF
RMSE (m)	1.16	1.08	1.10	0.81
R^2	0.73	0.78	0.75	0.87
MAE	0.80	0.76	0.78	0.50

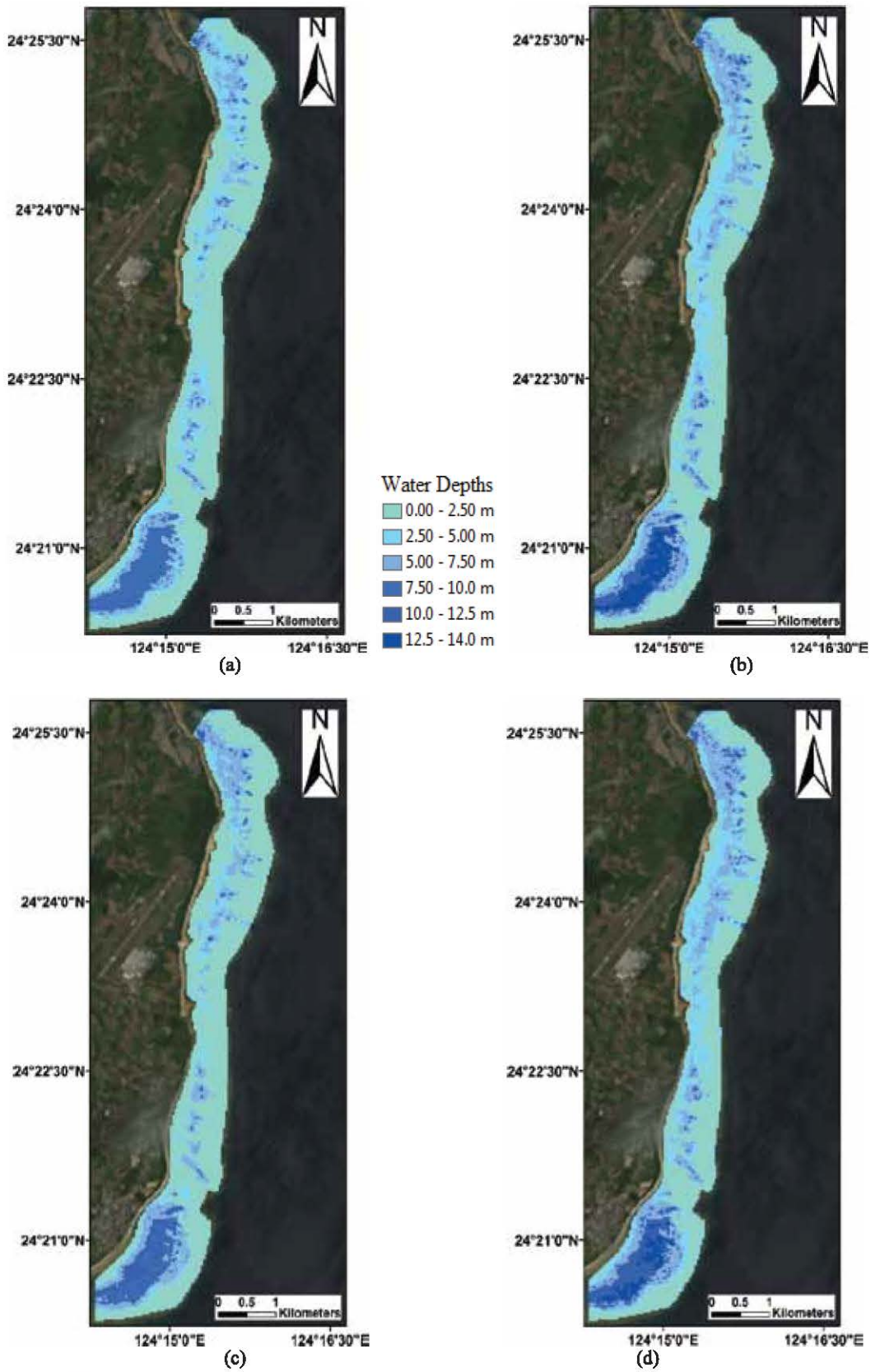

Figure 11: Bathymetric maps derived by applying each algorithm using Landsat-8 imagery over Shiraho Island area, Japan. (a) GLM (b) NN (c) MARS (d) RF

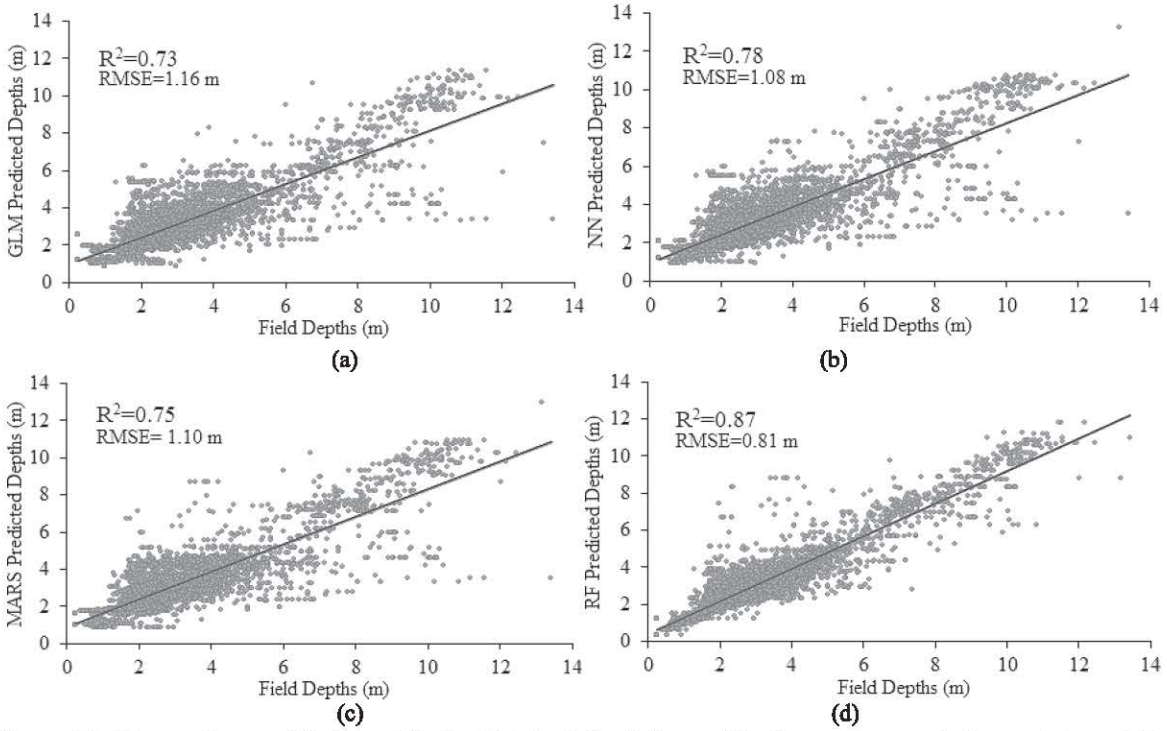

Figure 12: The continuous fitted models for Shiraho Island, Japan. Depths are represented as points, and the continuous line represents the continuous fitted model (a) GLM (b) NN (c) MARS (d) RF

Table 6: The RMSEs (in meters) of all bathymetry detection methods in three ranges of depths for Shiraho Island, Japan

Methodology	GLM	NN	MARS	RF
0-5 m	0.89	0.83	0.86	0.71
5-10 m	1.43	1.17	1.24	1.05
10-14 m	2.14	1.76	1.93	1.13

5. Discussion

To select the appropriate bands for bathymetry detection, a statistical analysis was performed to investigate the correlation between water depths and Landsat as well as Spot imageries bands. This investigation demonstrated a strong correlation between the red and green bands with water depths (Doxani et al., 2012 and Sánchez-Carnero et al., 2014). Besides the red and green bands, the blue/red and green/red band ratios also demonstrated a strong correlation to the water depths.

The Lyzenga GLM model correlates the band combination directly to the water depth. In our experiments, the best combination that achieved the lowest RMSE and highest R^2 values occurred between the green and red band logarithms as well as the blue/red and green/red band ratios. Also, NNs were used to perform a correlation between the multilayers of the imagery bands as an input and water depth as an output through multidimensional nonlinear functions. Our results agree well with those of previous studies such as Ceyhun and Yalçın (2010) and Gholamalifard et al., (2013), which have supported that NNs outperform conventional models as the Lyzenga GLM model or the Stumpf ratio model. An NN suffers from one major issue in that it requires many trials to find the best weights for correlation as it is an unstable black-box approach having significant fluctuations in RMSE and R^2 values from one trial to another.

The MARS algorithm, on the other hand, is a stable approach that avoids overfitting and achieves comparable results to NN in the study areas. After several trials, the optimum number of BFs and GCVs were selected on the basis of the minimum RMSE and maximum R^2.

For applying RF algorithm the optimum number of regression trees was selected after sequential trials of various numbers of trees, following which the best values were achieved with 50 decision trees. Also, the Gini diversity index was used for the

splitting trees that were not pruned. Two RF regression tree ensembles were created and combined. The randomness of the regression trees and the splitting of the data into training and testing sets ensured that the ensembles did not overfit the input data.

To compare the obtained results with previous results from comparable studies, image pixel sizes, water-quality levels, bottom cover nature, availability of adequate field points for each study area, and depth range should be considered. For instance, Sánchez-Carnero et al., (2014) confirmed the outperformance of Lyzenga GLM compared to principal component analysis (PCA) and green band correlation algorithms using Spot 4 imagery with 10 m resolution over turbid water in a shallow coastal area. The GLM yielded RMSE of 0.88 m in a depth range of 6 m. Pacheco et al., (2015) tested the Landsat 8 coastal, blue, and green bands for bathymetry detection using Lyzenga GLM over clear waters in a shallow coastal area and achieved an RMSE of 1.01 m in a depth range of 12 m. Also, Gholamalifard et al., (2013) supported the better performance of the NN approach compared to PCA and a red band correlation using Landsat 5 imagery over a deep water area. The research produced RMSE of 2.14 m in a depth range of 45 m. Our results are comparable to those of the studies for the NN and Lyzenga GLM approaches within the same depth ranges. In addition, the MARS and RF algorithms have been shown to outperform Lyzenga GLM. Finally, the RF ensemble has been shown to outperform the NN approach and provide more stability for three different sea bottom zones with a variable number of field points.

6. Conclusions

This paper proposed RF and MARS as new approaches for bathymetry detection. These approaches were applied in three diverse areas with different numbers of available field points: a low turbidity, deep, silt-sand bottom area of Alexandria port, Egypt, with depths of up to 10.5 m; a high-turbidity, clay bottom area of the Lake Nubia entrance zone, Sudan, with 6 m water depth; and a low-turbidity coral reef area of Shiraho Island, Japan, with 14 m water depth. The proposed approaches used green and red band logarithms alongside blue/red and green/red band ratios. These input data from the Landsat 8 and Spot 6 satellite images were corrected from atmospheric and sun-glint systematic errors, whereas water depths were the outputs. To validate the proposed approaches, they were compared with the Lyzenga GLM and NN approaches. All results were also compared with the echosounder field data for water depths.

The Lyzenga GLM correlation algorithm gave RMSE values of 0.96 m, 1.02 m, and 1.16 m, whereas the NN yielded RMSE values of 0.92 m, 0.96 m, and 1.08 m in the three study areas, respectively.

The proposed approaches, MARS, and RF produced RMSE values of 0.84 m and 0.64 m for the first study area, 0.98 m and 0.84 m for the second study area, and 1.10 m and 0.81 m for the third study area, respectively. From these results, it can be concluded that RF and MARS provide more accurate results than Lyzenga GLM for bathymetry mapping over a diverse range of areas. Moreover, the RF model has been shown to outperform the NN approach in this context.

Acknowledgements

The first author would like to thank the Egyptian Ministry of Higher Education and Tokyo Institute of Technology, Nadaoka Laboratory for their support and offering the tools needed for this research.

References

Adam, E., Onisimo, M., John, O. and Elfatih, M., 2014, Land-Use/Cover Classification in a Heterogeneous Coastal Landscape using RapidEye Imagery: Evaluating the Performance of Random Forest and Support Vector Machines Classifiers. *International Journal of Remote Sensing*, 35(10): 3440–3458.

Berk, A., Bernstein, L., Anderson, G., Acharya, P., Robertson, D., Chetwynd, J. and Adler-Golden, S., 1998, MODTRAN Cloud and Multiple Scattering Upgrades with Application to AVIRIS. *Remote Sensing of Environment*, 65(3): 367–375.

Blakey, T., Melesse, A. and Hall, M., 2015, Supervised Classification of Benthic Reflectance in Shallow Subtropical Waters using a Generalized Pixel-Based Classifier across a Time Series. *Remote Sensing*, 7(5): 5098–5116.

Bramante, J. F., Raju, D. K. and Sin, T. M., 2013, Multispectral Derivation of Bathymetry in Singapore's Shallow, Turbid Waters. *International Journal of Remote Sensing*, 34(6): 2070–2088.

Breiman, L., 2001, Random Forests. *Journal of Machine Learning*, 45(1): 5–32.

Ceyhun, Ö. and Yalçın, A., 2010, Remote Sensing of Water Depths in Shallow Waters via Artificial Neural Networks. *Estuarine, Coastal and Shelf Science*, 89(1): 89–96.

Chust, G., Grande, M., Galparsoro, I., Uriarte, A. and Borja, Á., 2010, Capabilities of the Bathymetric Hawk Eye LiDAR for Coastal Habitat Mapping: A Case Study within a Basque Estuary. Estuarine, *Coastal and Shelf Science*, 89(3): 200–213.

Collin, A., Nadaoka, K. and Nakamura, T., 2014, Mapping VHR Water Depth , Seabed and Land Cover Using Google Earth Data. *ISPRS International Journal of Geo-Information*, 3: 1157–1179.

Conoscenti, C., Ciaccio, M., Caraballo-Arias, N., Gómez-Gutiérrez, Á., Rotigliano, E. and Agnesi, V., 2015, Assessment of Susceptibility to Earth-Flow Landslide using Logistic Regression and Multivariate Adaptive Regression Splines: A Case of the Belice River Basin (Western Sicily, Italy). *Geomorphology*, 242: 49–64.

Corucci, L., 2011, Approaching Bathymetry Estimation from High Resolution Multispectral Satellite Images using a Neuro-Fuzzy Technique. *Journal of Applied Remote Sensing*, 5(1): 1-15.

Doxani, G., Papadopoulou, M., Lafazani, P., Pikridas, C. and Tsakiri-Strati, M., 2012, Shallow-Water Bathymetry over Variable Bottom Types using Multispectral Worldview-2 Image. International Archives of the Photogrammetry, *Remote Sensing and Spatial Information Sciences*, 39(B8): 159–164.

Emamgolizadeh, S., Bateni, S. M., Shahsavani, D., Ashrafi, T. and Ghorbani, H., 2015, Estimation of Soil Cation Exchange Capacity using Genetic Expression Programming and Multivariate Adaptive Regression Splines. *Journal of Hydrology*, 529: 1590–1600.

Friedman, J. H., 1991, Multivariate Adaptive Regression Splines. *The Annals of Statistics*, 19(1): 1–141.

Gao, J., 2009, Bathymetric Mapping by Means of Remote Sensing : Methods, Accuracy and Limitations. *Progress in Physical Geography*, 33(1): 103–116.

Gentle, J., Härdle, W. and Mori, Y., 2012, Generalized Linear Models. In Handbook of Computational Statistics: Concepts and Methods, Springer Handbooks of Computational Statistics, *Springer Berlin Heidelberg*. book, 681–709.

Ghimire, B., Rogan, J., Rodriguez-Galiano, V., Panday, P. and Neeti, N., 2012, An Evaluation of Bagging , Boosting and Random Forests for Land-Cover Classiication in Cape Cod, Massachusetts, USA. *GIScience & Remote Sensing*, 5(5): 623–643.

Gharineiat, Z. and Deng, X., 2015, Application of the Multi-Adaptive Regression Splines to Integrate Sea Level Data from Altimetry and Tide Gauges for Monitoring Extreme Sea Level Events. *Marine Geodesy*, 38(3): 261–276.

Gholamalifard, M., Kutser, T., Esmaili-Sari, A., Abkar, A. and Naimi, B., 2013, Remotely Sensed Empirical Modeling of Bathymetry in the Southeastern Caspian *Sea. Remote Sensing*, 5(6): 2746–2762.

Guan, H., Yu, J., Li, J., and Luo, L., 2012, Random Forests-Based Feature Selection for Land-Use Classification using Lidar Data and Orthoimagery. *XXII ISPRS Congress*, XXXIX: 203–208.

Haleem, K., Gan, A. and Lu, J., 2013, Using Multivariate Adaptive Regression Splines (MARS) to Develop Crash Modification Factors for Urban Freeway Interchange Influence Areas. *Accident Analysis and Prevention*, 55: 12–21.

Hastie, T., Tibshirani, R. and Friedman, J., 2009, Springer Series in Statistics. The Elements of Statistical Learning Data Mining, Inference, and Prediction. Stanford, California: *Springer Series in Statistics*.(2nd Ed.):321–335.

Hedley, J., Harborne, A. and Mumby, P., 2005, Technical Note: Simple and Robust Removal of Sun Glint for Mapping Shallow water Benthos. *International Journal of Remote Sensing*, 26(10): 2107–2112.

Heyman, W. D., Ecochard, J. B. and Biasi, F. B., 2007, Low-Cost Bathymetric Mapping for Tropical Marine Conservation—A Focus on Reef Fish Spawning Aggregation Sites. *Marine Geodesy*, 30: 37–50.

Jekabsons, G. 2016, ARESLab: Adaptive Regression Splines Toolbox for Matlab/Octave. : 1–19.

Kay, S., Hedley, J. and Lavender, S., 2009, Sun Glint Correction of High and Low Spatial Resolution Images of Aquatic Scenes: A Review of Methods for Visible and Near-Infrared Wavelengths. *Remote Sensing*, 1(4): 697–730.

Kim, H. and Sohn, G., 2011, Random Forests Based Multiple Classifier System for Power-Line Scene Classification. *International Archives of the Photogrammetry*, XXXVIII: 29–31.

Kisi, O. and Parmar, K., 2016, Application of Least Square Support Vector Machine and Multivariate Adaptive Regression Spline Models in Long Term Prediction of River Water Pollution. *Journal of Hydrology*, 534: 104–112.

Kuter, S., Akyürek, Z. and Weber, W., 2016, Estimation of Subpixel Snow-Covered Area by Nonparametric Regression Splines. International

Archives of the Photogrammetry, *Remote Sensing and Spatial Information Sciences*, XLII-2-W1: 31–36.

Landsat-8. 2013, Using the USGS Landsat 8 Product. Available from: http://landsat.usgs.gov/Landsat8_Using_Product.php (January 20, 2016).

Leu, L. and Chang, H., 2005, Remotely Sensing in Detecting the Water Depths and Bed Load of Shallow Waters and Their Changes. *Ocean Engineering*, 32(10): 1174–1198.

Lyons, M., Phinn, S. and Roelfsema, C., 2011, Integrating Quickbird Multi-Spectral Satellite and Field Data: Mapping Bathymetry, Seagrass Cover, Seagrass Species and Change in Moreton Bay, Australia in 2004 and 2007. *Remote Sensing*, 3(12): 42–64.

Lyzenga, D. R., 1985, Shallow-Water Bathymetry using Combined Lidar and Passive Multispectral Scanner Data. *International Journal of Remote Sensing*, 6(1): 115–125.

Lyzenga, D. R., Malinas, N. P. and Tanis, F. J., 2006, Multispectral Bathymetry using a Simple Physically Based Algorithm. *IEEE Transactions on Geoscience and Remote Sensing*, 44(8): 2251–2259.

Mather, P. and Tso, B., 2009, Artificial Neural Networks. In Classification Methods for Remotely Sensed Data. CRC Press. (2nd Ed.):77–124.

Moses, S., Janaki, L., Joseph, S., Gomathi, J. and Joseph, J., 2013, Lake Bathymetry from Indian Remote Sensing (P6-LISS III) Satellite Imagery using Artificial Neural Network Model. Lakes & Reservoirs: *Research & Management*, 18(2): 145–153.

Pacheco, A., Horta, J., Loureiro, C. and Ferreira, Ó., 2015, Retrieval of Nearshore Bathymetry from Landsat 8 Images: A Tool for Coastal Monitoring in Shallow Waters. *Remote Sensing of Environment*, 159: 102–116.

Ranganathan, A., 2004, The Levenberg-Marquardt Algorithm. *Internet httpexcelsior cs ucsb educoursescs*, 142: 1–5.

Razavi, B., 2014, Predicting the Trend of Land Use Changes using Artificial Neural Network and Markov Chain Model (Case Study: Kermanshah City). *Research Journal of Environmental and Earth*, 6(4): 215–226.

Rumelhart, D. E., Hinton, G. E. and Williams, R. J., 1986, Learning Internal Representations by Error Propagation. In Parallel Distributed Processing: Explorations in the Microstructure of Cognition. PDP Research Group. Cambridge, MA, USA: MIT Press. (1st Ed.):318–362.

Sánchez-Carnero, N., Ojeda-Zujar, J., Rodríguez-Pérez, D. and Marquez-Perez, J., 2014, Assessment of Different Models for Bathymetry Calculation using SPOT Multispectral Images in a High-Turbidity Area: The Mouth of the Guadiana Estuary. *International Journal of Remote Sensing*, 35(2): 493–514.

Sonobe, R., Hiroshi, T., Xiufeng, W., Nobuyuki, K., and Hideki, S.., 2014, Random Forest Classification of Crop Type using Multi-Temporal TerraSAR-X Dual-Polarimetric Data. Remote Sensing Letters, 5(2): 157–164.

Stumpf, R., Holderied, K. and Sinclair, M., 2003, Determination of Water Depth with High-Resolution Satellite Imagery over Variable Bottom Types. *Limonology and Oceanography*, 48: 547–556.

Su, H., Liu, H. and Heyman, W., 2008, Automated Derivation of Bathymetric Information from Multi-Spectral Satellite Imagery using a Non-Linear Inversion Model. *Marine Geodesy*, 31: 281–298.

Updike, T. and Comp, C., 2010, Radiometric use of WorldView-2 Imagery Technical Note 1 WorldView-2 Instrument Description. Available from: http://global.digitalglobe.com/sites/default/files/Radiometric_Use_of_WorldView 2_Imagery (1).pdf.

Wahidin, N., Siregar, V., Nababan, B., Jaya, I. and Wouthuyzen, S., 2015, Object-Based Image Analysis for Coral Reef Benthic Habitat Mapping with Several Classification Algorithms. *Procedia Environmental Sciences*, 24: 222–227.

Vahtmäe, E. and Kutser, T., 2016, Airborne Mapping of Shallow Water Bathymetry in the Optically Complex Waters of the Baltic Sea. *Journal of Applied Remote Sensing*, 10(2): 1–16.

Zhang, W. and Goh, A., 2013, Multivariate Adaptive Regression Splines for Analysis of Geotechnical Engineering Systems. *Computers and Geotechnics*, 48: 82–95.

Zhang, W., Goh, A., Zhang, Y., Chen, Y. and Xiao, Y., 2015, Assessment of Soil Liquefaction Based on Capacity Energy Concept and Multivariate Adaptive Regression Splines. *Engineering Geology*, 188: 29–37.

Zhou, Y. and Leung, H., 2007, Predicting Object-Oriented Software Maintainability using Multivariate Adaptive Regression Splines. *Journal of Systems and Software*, 80(8): 1349–1361.